ENHANCEMENTS IN MAAP5.03+ MCCI AND CORIUM COOLABILITY MODELS AND BENCHMARKS AGAINST OECD CCI TESTS

Quan Zhou*, Chan Y. Paik, and Paul B. McMinn
Fauske & Associates, LLC
16W070 83rd st, Burr Ridge, IL, 60527, U.S.A.
zhou@fauske.com; paik@fauske.com; mcminn@fauske.com

ABSTRACT

Molten Corium-Concrete Interaction (MCCI) and corium coolability (heat transfer between corium and overlying water pool) are modeled as part of the containment model in the MAAP 5 code. MAAP5.03+ (an alpha version of what will eventually become MAAP5.04) has added bulk cooling as one of the corium coolability mechanisms. There were two mechanisms modeled in previous versions of the code: water ingression and melt eruption. This paper discusses the features of the MCCI and corium coolablity models in MAAP5, and presents the benchmark results of comparisons of MAAP5.03+ against two tests in the OECD/CCI test series: CCI-2 and CCI-3. It discusses the comparisons with and without the bulk cooling model to demonstrate the performance of the models.

KEYWORDS
MCCI, CCI Test, MAAP5, Coolability, Benchmark

1. INTRODUCTION

Molten Corium-Concrete Interaction (MCCI) is a phenomenon that may occur in the containment of a nuclear power plant during a severe accident. It poses a threat to the containment integrity because MCCI can cause continuous containment pressurization and sustained concrete structure damage. For most PWR and BWR plants, flooding the reactor cavity (PWR) or pedestal (BWR) in the containment is the only way to mitigate the effects of MCCI. A key success criterion for flooding is that the heat transfer rate from corium to water is sufficiently large to terminate the concrete decomposition, and eventually keep the corium at low temperature. The heat transfer rate depends on various heat transfer mechanisms that are commonly referred to as coolability mechanisms. Farmer et al. [1] has identified four major coolability mechanisms observed in MCCI experiments. These are: bulk cooling, melt eruption, water ingression, and crust breach. Bulk cooling is a short term cooling mechanism that occurs for several minutes after water addition. Melt eruption and water ingression are long term cooling mechanisms that determine the progression of MCCI for most cases. Crust breach is a mechanism that may re-invigorate the other three mechanisms. The effectiveness of the coolability mechanisms is determined by a number of plant and scenario specific factors, including the containment design, the amount and decay power in the corium in the containment, and the timing of flooding. Typically, detailed analyses with severe accident computer code are required to assess the ability to cool the debris by flooding.

Modular Accident Analysis Program (MAAP) is a severe accident code developed and maintained by Fauske and Associates, LLC (FAI) as a contractor to Electrical Power Research Institute (EPRI). It has been used by the nuclear industry for severe accident and safety related analyses for three decades. MAAP provides the capability to simulate severe accident phenomena, including MCCI and corium

coolability, for different plant designs and accident scenarios. The corium coolability model in MAAP has been improved extensively in several recent MAAP releases. Specifically, two mechanistic models have been added in MAAP5.02 to model water ingression and particle bed generation by melt eruption. A new model has been added in MAAP5.03+ (which will eventually become the next release, MAAP5.04) to model bulk cooling. The last coolability mechanism identified by Farmer et al. [1], namely crust breach, is considered a phenomenon more relevant to experiment scale analysis. At plant scale, the upper crust is most likely a "floating" crust, with little potential to attach to the sidewall. The is because of the large lateral span at plant scale and weak strength of the crust [1]. Therefore, the crust breach mechanism is ignored in the MAAP code. In addition to the coolability model, a new corium shape model was also added in the MAAP5.03+ code to allow the simulation of the evolvement of the shape of the corium-concrete interface.

The purpose of this paper is to discuss all three coolability models in MAAP5.03+, and present the latest benchmark results comparing MAAP5.03+ against two large scale OECD/NEA MCCI tests: CCI-2 and CCI-3 [2]. Although similar benchmarks have been performed for the water ingression and melt eruption models in MAAP5.02 code [3] previously, the latest benchmarks are the first to consider all three coolability models. Also, the benchmarks for MAAP5.02 were performed with an overly large heating power after water addition. The objective of this work is to examine the capabilities of the latest MAAP code to perform MCCI and corium coolability analyses in nuclear power plants. Section 2 of this paper discusses the models, Section 3 briefly summarizes the CCI tests, Section 4 presents and discusses the benchmark results, and Section 5 presents the conclusions drawn from the comparisons of code results to experimental data.

2. CORIUM COOLABILITY AND SHAPE MODELS IN MAAP5.03+

2.1. Bulk Cooling Model

Bulk cooling is a decomposition gas enhanced film boiling that has been observed in a number of "wet" MCCI experiments [1]. This phenomenon occurs when flooding is delayed for a period of time after corium is relocated into the containment. If flooding is delayed, the corium temperature will be high enough to support film boiling at the top at the time that flooding is initiated. If the corium surface is crust free, and concrete decomposition is occurring, the gas bubbles from concrete decomposition can increase the film boiling heat transfer by deforming the area, and impeding the crust formation. This cooling mechanism is a short term mechanism, but the heat flux during bulk cooling can be very high.

Farmer et al [4] [5] have developed a bulk cooling model to address the high heat fluxes observed in experiments. The bulk cooling model in MAAP5.03+ is a variant of Farmer's model. The differences exist mainly in two areas: a) the effects of gases in Farmer's model are counted for both area deformation and conduction through the film, while in MAAP model only counted for the area deformation; b) the criterion of stable crust formation in Farmer's model is based on a circular disk without deflection, while the criterion in the MAAP model is based on an infinite large crust with upward deflection. The first change was made because the effect of gases on the conduction heat transfer is expected to be very small, and ignoring it can significantly reduce the complexity of the model. The second change was made because using a criterion based on upward deflection eliminates the need for one of the modeling parameters.

The MAAP model assumes that heat transfer from the corium to water occurs through radiation and thermal conduction across the vapor and gas film separating the corium from water. Since the effect of gases is ignored, the thermal conduction heat flux q''_B, in the absence of gas sparging, is given by the classical Berenson [6] heat flux:

$$q''_B = 0.425\left\{k_g^3\left[h_{lg} + 0.5c_g(T_{cm} - T_{sat})\right]/(\mu_g \lambda)\right\}^{\frac{1}{4}}(T_{cm} - T_{sat})^{\frac{3}{4}} \quad (1)$$

where λ is the Taylor wavelength (without the numerical coefficient). k_g, c_g, μ_g and h_{lg} are steam conductivity, specific heat, viscosity, and vaporization latent heat. T_{cm} is the corium temperature, and T_{sat} is the water saturation temperature. The radiation heat flux q''_{rad} is given by $q''_{rad} = \epsilon\sigma(T_{cm}^4 - T_{sat}^4)$, where ϵ is the corium emissivity and σ is the Stefan-Boltzmann constant. The total heat flux q" due to both radiation and conduction, but no gas sparging, follows the combining law proposed by Bromley [7]:

$$q''/q''_B = (q''_B/q'')^{\frac{1}{3}} + (q''_{rad}/q''_B) \quad (2)$$

Farmer et al. [4] models a MCCI-pool-surface-area increase due to gas sparging. The dimensionless area enhancement factor A^*, defined as the ratio of the real heat transfer area to the flat surface area, is given by $A^* = 1 + 4.5 \cdot j_g/U_T$, where j_g is the superficial velocity of the rising decomposition gases and U_T is the terminal rise velocity of a gas bubble. The heat flux with the area increase effect due to sparging gas is thus $q''_{BC} = A^* \cdot q''$.

As the corium temperature and gas flow rate drop, the non-condensable gases eventually are unable to prevent the formation of a stable upper crust. The incipience of the stable crust marks the termination of bulk cooling. According to Farmer et al. [5], the critical gas superficial velocity, below which the crust will form, is represented by

$$j_{g,crit} = 0.445\, R/(\rho_{cr}\Delta e_{cr}\delta_{crit}) \cdot [q'' - h_m(T_{cm} - T_{mp,cr})] \quad (3)$$

where R is the bubble radius, and ρ_{cr}, Δe_{cr}, and $T_{mp,cr}$ are crust density, latent heat of fusion, and melting temperature. h_m is the heat transfer coefficient from molten corium to upper crust bottom surface. In MAAP5.03+, the correlation suggested by Deckwer [8] was used to evaluate the value of $h_m = 0.1\, k_m\left(j_g g/(\nu_m \alpha_m^2)\right)^{1/4}$, where g is the gravity acceleration, and k_m, ν_m, and α_m are thermal conductivity, kinematic viscosity, and thermal diffusivity of corium.

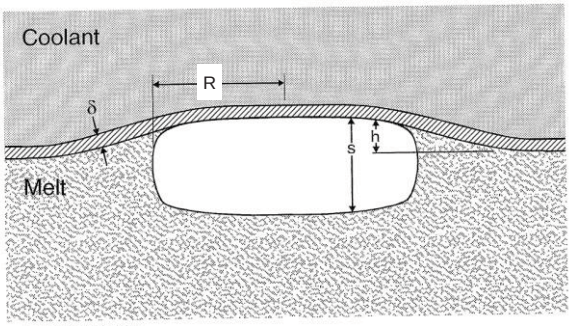

Figure 1. Topham's Model [9] of Crust Deflection due to a Cylindrical Bubble.

δ_{crit} in Eq. (3) is the critical thickness of the crust that will survive the static pressure load imposed by a single gas bubble. The model of crust stability in MAAP5 is based on Topham's study [9], as illustrated in Fig. 1, on an infinitely large crust deflecting upwards by a depth of h due to the pressure load imposed by a cylindrical bubble of radius R and depth s. The key in this model is that the deflection reduces the net force imposed by the bubble, because the net force is given by $F = (\rho_{cm} - \rho_g)g(s - h)\pi R^2$.

Therefore, the bending stress within the crust is smaller than the stress if no deflection is assumed. If the bending stress in the crust is less than its fracture stress, the crust is determined to survive. The MAAP5 model takes the numerical results from Topham's calculations, and correlates the dimensionless critical crust thickness Δ as a function of a dimensionless parameter B of the crust properties:

$$\Delta = 3.33B/(1 + 5.43B^{6/5})^{1/2} \tag{4}$$

where $\Delta = (E/(12(1-\nu^2)R^4 g\rho_{cr}))^{1/3}\delta_{crit}$; and $B = E/(12R(1-\nu^2))(g\rho_{cr}s^3/\sigma^3)^{1/2}$. In the definitions, E, σ and ν are elastic modulus, fracture stress and Poisson's ratio of the crust. The depth of the bubble is assumed to be s = (4/3)R. Such a change enables the model in MAAP5.03+ to not need additional modeling parameter adjustment related to the crust bending stress.

2.2. Water Ingression Model

After a stable crust is formed, heat transfer from corium to water transitions from bulk cooling to water ingression. Water ingression occurs due to the formation of cracks in the solidified crust at the top of the corium pool. The cracks allow water to penetrate deeper into the crust, permitting the heat flux from the corium to far exceed the conduction heat flux through the entire thickness of the crust. A model has been developed by Epstein [10] based on even earlier work by Lister [11]. However, this model did not consider the decay heat generation within the upper crust.

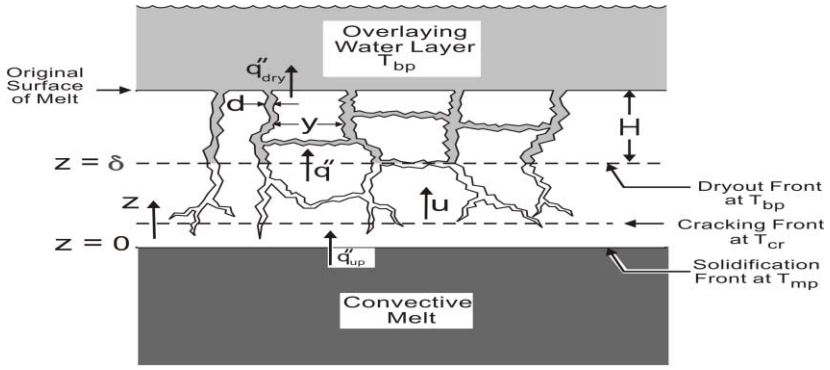

Figure 2. Illustration of Water Ingression Problem.

The water ingression model in MAAP5.03+ is an extension to Epstein's model [10] with the consideration of the internal heat generation in the crust. It is illustrated in Fig. 2. The cracks are expected to extend to certain depth from the top of the upper crust, but not all the way to the interface between molten corium and the crust. As the water penetrates into cracks, it can cool the upper part of the crust, but as the liquid water dries out, the lower part cannot be cooled effectively. Therefore, the upper crust is modeled as three regions: the topmost region is the wet region where liquid water and steam in the cracks keep the corium cooled. The middle region is the dry region where the cracks are filled by superheated steam, and the corium temperature is high. The bottom region is the crack-free region where the crust is solid, and the corium temperature is the highest. A basic assumption of the water ingression model is that all three regions move downward at the same corium quenching speed "u". The heat conduction equation in the dry and crack free regions $0 < z < \delta$ (see Fig. 2) is given by

$$u\frac{dT}{dz} = \alpha\frac{d^2T}{dz^2} + \frac{Q}{\rho \cdot c} \tag{5}$$

where α, ρ, and c are thermal diffusivity, density and specific heat of the crust, and Q is the volumetric heat generation rate. For given boundary conditions at z=0, and z=δ (check [10] for details), Eq. (5) can be solved, and the solution leads to the heat flux q" at the dry-out front z=δ as a function of u and the convective heat flux $q"_{up}$ at z=0:

$$\rho u\left[c\left(T_{mp,cr}-T_{sat}\right)+\Delta e_{cr}\right]+\frac{Q\alpha}{u}\ln\left(\frac{\frac{Q\alpha}{u}+q"}{\frac{Q\alpha}{u}+q"_{up}+\Delta e_{cr}\cdot\rho\cdot u}\right)=q"-q"_{up} \tag{6}$$

Since the wet region is cooled by liquid water and steam, it is reasonable to assume the decay power in the wet region is completely transferred to the water. The heat flux $q"_{dry}$ at top of the crust is thus given by

$$q"_{dry}=q"+Q\cdot H \tag{7}$$

where H is the wet region thickness. On the other hand, laboratory studies on heat transfer in porous media have shown that the heat flux $q"_{dry}$ can be represented by a function of permeability κ in the media , as

$$q"_{dry}=F\cdot h_{lg}\cdot\kappa\cdot(\rho_w-\rho_g)g/\nu_g \tag{8}$$

where ρ_w is water density, and F is a function of water and steam viscosities, accounting for the pressure effect on the thermodynamic properties of water and steam. At atmospheric pressure, the value of F is close to 0.51. Lister [11] has developed a one-dimensional model of the penetration of water into a propagating matrix of cracks in hot rock. The model shows that the permeability can be correlated by the axial temperature gradient at the cracking front, where the temperature is equal to a cracking temperature T_{cr}, (see Fig. 2):

$$\kappa=\frac{\sqrt{2}}{12}\left[\alpha_T(T_{cr}-T_{sat})\right]^3\left(-\frac{3.2\cdot\alpha\cdot\phi}{u\cdot(dT/dz)_{T_{cr}}-Q/(\rho\cdot c)}\right)^{4/5} \tag{9}$$

where α_T is the linear thermal expansion coefficient of crust, and ϕ is a model parameter. According to Lomperski and Farmer [12], the value of ϕ is close to 280 for fully oxidized corium. The final solution of the water ingression problem must follow an iterative approach: an initial guess of quenching speed u is made first.. The temperature gradient $(dT/dz)_{Tcr}$ at the cracking front is evaluated next, based on the solution of Eq. (5). The permeability, the heat flux $q"_{dry}$ and q" are evaluated with Eq. (7) through (9). The values of u, $q"_{dry}$ and q" are substituted into Eq. (6). If the left and right hand sides of Eq. (6) are equal or very close, the solution of heat fluxes has been found. Otherwise, a new value of u is evaluated using the Newton-Raphson method.

2.3. Particle Bed and Melt Eruption Model

The formation of a particle bed can transform corium geometry from a non-coolable continuous bed to a coolable configuration. This cooling mechanism can occur through-out the entire duration of MCCI. As illustrated in Fig. 3(a) and (b), two mechanisms are identified to generate a particle bed in a nuclear power plant environment: corium jet breakup, and melt eruption. The former occurs when the corium is relocated into a cavity pre-flooded by water, where violent fuel-water interaction (FCI) strips off a large number of particles from the corium jet. The particles settle on top of the continuous corium pool formed by the remaining un-broken corium jet (if any). The latter occurs when the concrete under the corium

pool decomposes. The gases released from the concrete decomposition entrain mass from the continuous pool to the water and form the particle bed.

The amount of particles formed during corium jet breakup is calculated based on the entrainment similarity assumption [13]. Under this assumption, the thinning speed of the corium jet radius is similar to the entrainment correlation proposed by [14], and can be written as

$$dr/dt = -0.045 \cdot u_{dj} \left(\rho_w/\rho_{cm}\right)^{0.5} \tag{10}$$

where u_{dj} is the jet velocity, and r is the corium jet radius. Assuming that the jet velocity is invariant, one finds that the jet radius decreases linearly along the path through the water pool. The amount of particles generated during the jet breakup is given by the difference between the total relocated corium mass and the mass carried by the unbroken corium jet when it touches the concrete floor.

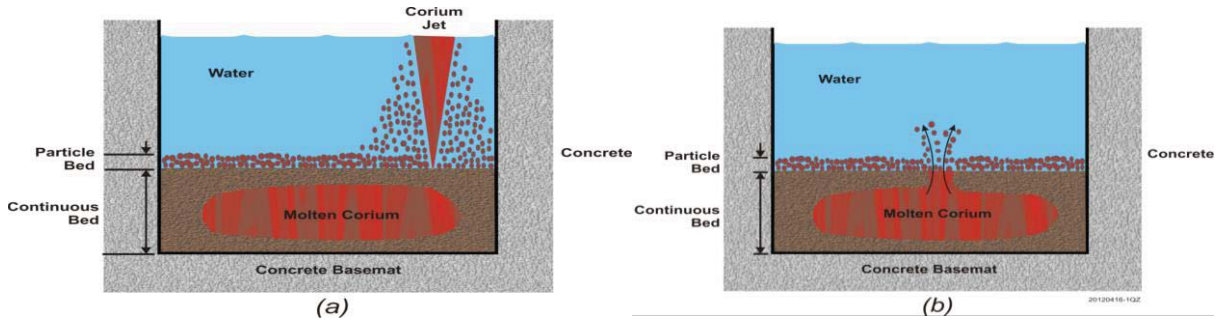

Figure 3. Particle Bed Generation: a) through Corium Jet Breakup; b) through Melt Eruption.

Melt eruptions may occur when gas from the underlying decomposing concrete entrains the melt and transports it through a breach in the corium pool's crust cover. Although most melt eruptions observed in experiments are sporadic events, it was found that the total amount of particles generated through the eruptions can be reasonably correlated through the continuous entrainment correlation suggested in [14]. The rate of the particles generated is given by

$$dm_{pb}/dt = E_0 \cdot W_g \left(\rho_{cm}/\rho_g\right)^{0.5} \tag{11}$$

where W_g is the flow rate of gases from concrete decomposition. To prevent generating particle bed for very small gas flow rates, a cut-off flow rate of 1.e-3 kg/s was imposed for W_g, in the above equation. The entrainment factor E_0 is a key parameter for the melt eruption model. According to simulant and prototypic material experiments, an E_0=0.08 provides a lower bound to the experiment data for the mass of corium entrained by melt eruptions.

MAAP5 calculates the critical heat transfer rate from particle bed to water based on either Lipinski's correlation [15] or Henry's correlation [16]. For the particle sizes generated through jet break-up or melt eruption (about a few millimeters to centimeters), these two correlations calculate the particle bed can be easily cooled by water.

3. CCI TESTS

Core Concrete Interaction (CCI) tests [2] are a series of experiments performed by Argonne National Laboratory (ANL) under the sponsorship of OECD/NEA. The test section of the CCI experiments is a

vessel with a square concrete basemat surrounded by four sidewalls. The east and west sidewalls of the vessel are made of non-ablating refractory material (MgO), which is further protected by a 2.5 cm layer of crushed UO_2 pellets and powder. The inner surfaces of the east and west sidewalls are lined with tungsten electrodes to provide heating power to the corium. The north and south sidewalls are made of the same concrete material as the basemat, and can be ablated during the experiment. In this sense, the CCI tests are considered "2-D" since they allow both basemat and sidewall ablation. The sidewalls and basemat are loaded with thermocouples (TCs) to measure thermal profiles in these structures. As the ablation occurs, these TCs provide the time when the temperature in the structures reaches the concrete ablation temperature. The information together with the location of the TCs can be used to re-construct the shape of the ablation front in the concrete.

MAAP5.03+ simulations have been performed to compare against two tests in the experiment series, CCI-2 and CCI-3. The reasons that these tests were chosen for comparisons are: a) the conditions in these tests including corium composition, test scale, and 2-D geometry are the most representative of plant conditions that the author is aware of; b) the concrete types in these tests include both the high gas content limestone-common sand (LCS) concrete, and low gas content siliceous concrete; and c) all four coolability mechanisms have been observed. A brief review of the test conditions follows. Details can be found in CCI test reports [2].

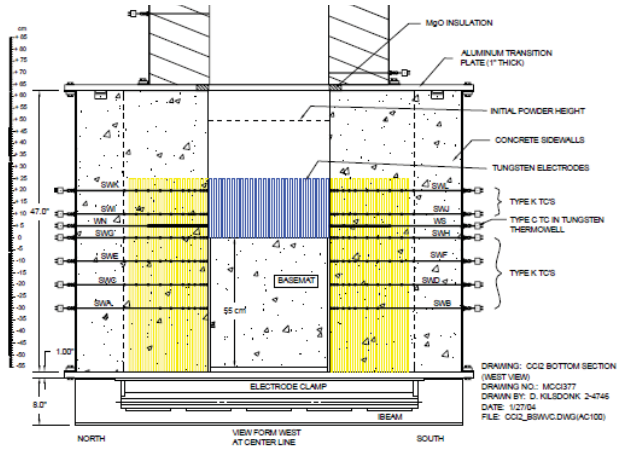

Figure 4. North-South Side View of the Lower Test Section for CCI-2 and CCI-3 Tests.

CCI-2 is the second experiment in the CCI series and was designed to investigate the interactions between fully oxidized corium and Limestone/Common Sand (LCS) concrete under dry and wet conditions. Fig. 4 shows the north-east side view of the test section. The dimension of the basemat is 50×50 cm. The basemat and sidewalls are made of LCS concrete with about 34% of gaseous constituents, including water (bonded and free) and CO_2. The test involves a total of 400 kg of fully oxidized corium generated through exothermal reactions in the test section. The generated corium is comprised of core oxides (UO_2, ZrO_2) and about 8% of LCS concrete materials to account for the ablation as the corium spreads on top of the reactor cavity floor. The test was conducted with constant heating power before the ablation reached 30 cm in the basemat or sidewalls. After it reached 30 cm, water was added into the test section and the heating mode was switched from constant power to constant voltage. The switch was made to maintain the same volumetric heating power in the molten part of the corium, because the heating method in the CCI tests can only heat-up the molten part effectively. The heat flux from corium to water was measured based on the condensed water mass in the experiment.

CCI-3 is the third test in the series and it investigates the interactions between corium and siliceous concrete. The test section of CCI-3 is identical to that of CCI-2. The difference between CCI-3 and CCI-2 is in the corium composition and the concrete material. The mass of the corium in the CCI-3 test (about 375 kg) is slightly less than the mass in the CCI-2 test (400 kg). The CCI-3 corium contains about 15% siliceous concrete. The concrete material for the floor and ablating sidewalls is the European type of siliceous concrete, which contains about 13.5% gas constituents.

4. BENCHMARK RESULTS

The electrical power in CCI tests was simulated by a decay power provided through the benchmark input in MAAP5.03+. As described in the previous section, the heating mode in CCI tests was switched from constant power to constant voltage after water addition. The switch resulted in a lower power after the water addition. The decay power in the MAAP model applies to both the molten part and the solidified parts. It is difficult to simulate the test condition in CCI-2, where the heat is only directed to the molten part of the corium. Previous benchmarks [3] for MAAP5.02 have used a constant decay heat throughout the simulations, i.e., no reduction of the power after the water addition. The argument was that the constant power would ensure constant volumetric heat generation in the molten corium. However, these previous calculations did not preserve the total energy input into the corium pool in the tests. The overly large heating power after water addition in these previous calculations actually caused larger heat fluxes to water, compared to experiment data. In light of this limitation, it was decided that in the current comparison, the total electrical power in the experiment should be used as input to the simulation, without trying to match the volumetric power in the molten part of the corium. The benefit of this method is that the total energy in the experiment is maintained. However, the volumetric heat generation in the molten part may be different from the experiment after water addition.

4.1. CCI-2 Test

Fig. 5(a) compares the electrical power used in the CCI-2 simulation to the decay power only in the molten part calculated by MAAP. Before the water addition, almost 100% of the corium is molten, and most heating power is added into the molten corium. After the water addition, the power generation in the molten corium is about 10 to 15 kW less than the heating power in the experiment for the case without the bulk cooling model (but with water ingression and melt eruption models). The power calculated with the bulk cooling model is even closer, about 2 to 10 kW less. Therefore, even if the MAAP model applies the decay power to all regions in the corium, the chosen heating methodology results in a good match of the heating power in the molten part.

Fig. 5(b) compares the temperature of the molten part of the corium calculated by MAAP5.03+ to the experiment data for cases with and without the bulk cooling model. In the first 3,500 seconds, the MAAP5 result shows that corium temperature increases from the initial temperature 2150 K to about 2500 K, and then starts to decrease. The experiment data do not show this temperature increase. Instead, the temperature starts to decrease from the initial 2150 K almost immediately. Before the water addition, MAAP5 over-predicts the corium temperature by about 100 to 300 K. The initial temperature increase and the over-prediction of the temperature indicate that the MAAP heat transfer coefficient from the corium to the surrounding crust is smaller than what is suggested by the experiment data. This issue has been discussed in [3].

After the water addition, the MAAP result without bulk cooling shows the temperature in the molten corium decreases gradually, due to quenching of the corium from the top. The MAAP result with bulk cooling shows a temperature dip caused by bulk cooling right after the water addition. The data in the experiment, however, suggest the temperature in the molten corium increases slightly after the water addition, and then starts to decrease. A possible explanation for this unexpected rise in corium

temperature is that the corium temperature in Fig. 5(b) is an envelope of the data recorded by all the thermal couples (TCs). After the water addition, the large heat transfer increased the solid fraction within the corium pool, and the molten and solid mass was at inhomogeneous and non-equilibrium condition, with the locally concentrated molten mass at a higher temperature. Since the temperature was actually slightly increasing, it may suggest that the crust formed around the molten mass acted as an insulation layer, and the worsening of heat transfer caused the temperature increase.

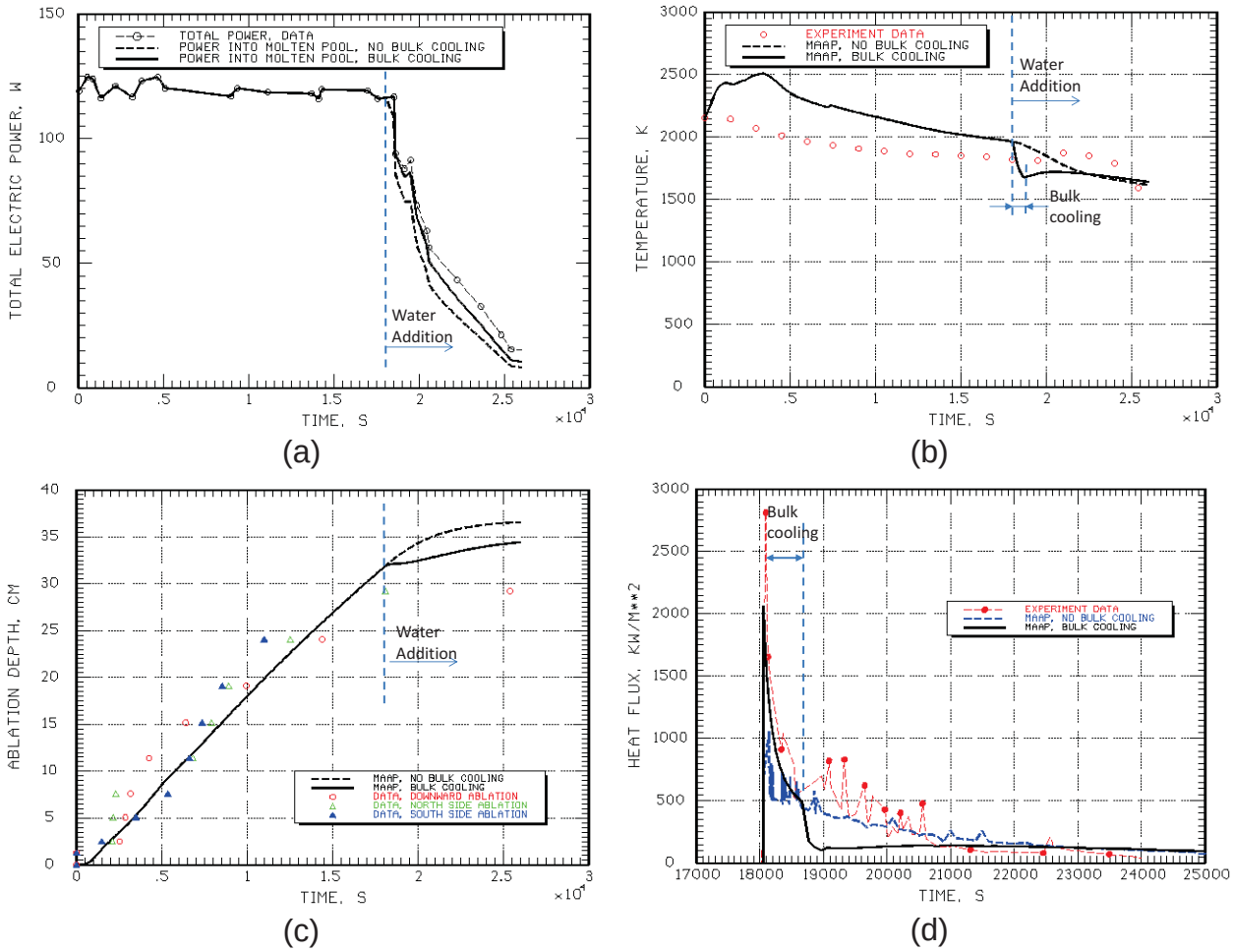

Figure 5. Comparisons of CCI-2 Test with and without bulk cooling model : (a) Heating power; (b) Corium temperature; (c) Ablation depth; (d) Heat flux to water.

Fig. 5(c) shows the comparisons of the ablation depths in the basemat and sidewalls. MAAP5.03+ calculated almost identical downward and sideward ablation rates because identical downward and sideward convective heat transfer coefficients were used for this test [3]. The experiment data show the ablation in the basemat and in the north sidewall was small until about 2500 s. However, after 2500 s, it progressed at a very rapid speed for about 500 s. The ablation then slowed down after 3000 s and progressed at a long term rate of about 0.01 mm/s. The delay of significant ablation and the following rapid ablation spike suggest that so-called refractory crusts (which is formed by solidified high melting temperature materials, UO_2 and ZrO_2) existed up to 2500 s, and were breached by thermal attack on the corium side and pressure buildup on the concrete side. MAAP does not model such refractory crusts, and the MAAP results show neither the initial ablation delay nor the rapid ablation rate after the delay.

However, the calculated average ablation rates before the water addition are reasonably close to the experiment data. After the water addition, experiment data shows the ablation decreased rapidly. MAAP calculation without bulk cooling shows a continuous but slower increase in the ablation depth after the water addition. The ablation rate does not flatten out until the ablation depth reaches about 36 cm, and the final ablation depth is about 7 cm larger than the experiment data. The MAAP calculation with bulk cooling shows a dramatic decrease of the ablation rate during the short bulk cooling period. However, after the bulk cooling time, the ablation rate picks up again, and the final ablation depth is about 5 cm larger than the experiment data.

Fig. 5(d) shows the comparison of heat flux from the corium to water between the MAAP calculation and experiment data. The peak heat flux without the bulk cooling model is about 1 MW/m^2, which is much lower than the peak heat flux of about 2.8 MW/m^2 recorded in the experiment. The no-bulk-cooling case exhibits many spikes between the time of water addition and around 19,000 s, which are caused by melt eruptions. The average heat flux due to melt eruption and heat transfer from the particulate bed to water is about 500 kW/m^2 in this short period, and it gradually decreases to almost zero at about 25,000 s. The heat flux due to water ingression is about 190 kW/m^2 after a very short (about 90 seconds) intensive heat transfer (due to film boiling). The heat flux due to water ingression decreases more slowly than the heat flux due to melt eruption. Even at the end of simulation, the heat flux due to the water ingression is still about 60 kW/m^2. The total long term heat flux due to melt eruption and water ingression (after 20,500 s) is slightly higher than the experiment data for this case. Compared to the previous comparison [3] which results in a long term heat flux almost twice as high as the experiment data, the agreement of the current comparison has been significantly improved.

Activating the bulk cooling model increases the peak heat flux from 1 MW/m^2 to about 2.1 MW/m^2. The general agreement during the bulk cooling phase, which lasts about 610 s, is reasonably good compared to the experiment. After bulk cooling, MAAP heat flux drops from 500 kW/m^2 to about 120 kW/m^2, and further to about 70 kW/m^2. Such a drop marks the transition of the heat transfer mechanism from bulk cooling and film boiling to water ingression. Experiment data show a similar total heat flux at the end of the bulk cooling. However, from the end time of bulk cooling to about 20,500 s, the data show that the heat flux fluctuates and the average heat flux is appreciably higher than the MAAP calculation. It is believed that the fluctuating high heat flux before 20,500 s is caused by melt eruption, since the CCI-2 experiment report [2] described that the video recorder installed at the top of the test section recorded "luminescence" caused by melt eruption during this period of time. However, the occurrence of the melt eruption seems contradictory to the bulk cooling physics and the ablation rate data. The bulk cooling terminates because the corium pool temperature drops and the concrete ablation is nearly arrested. In order to have strong melt eruption, there must be an active concrete ablation and build-up of the pressure below the upper crust. The contradiction might be explained again by the inhomogeneity of the corium pool after the water addition. As described before, the corium may be cold globally, but molten corium may be locally concentrated. The high temperature corium supports local concrete ablation and eruption. The ablation rate, although its value might be small, still caused a pressure build-up below the crust. Eventually, the pressure caused fractures in the crust and sporadic eruption events. The MAAP melt eruption model assumes that the melt eruption occurs continuously. It is incapable of simulating sporadic eruption events. Therefore, it only calculates a modest heat flux due to melt eruption about 60 kW/m^2 right after the bulk cooling, and it eventually reduces to zero. However, ignoring the sporadic eruptions due to the small but continuous ablation rates renders MAAP results more conservative.

In addition to the corium coolability models, MAAP5.03+ is also equipped with a shape model which allows the simulation of evolvement of the shape of the corium and concrete interface. Fig. 6 shows the comparison of the shape at the end of the CCI-2 simulation with the shape constructed from the thermocouple data and photos during post-experiment examination. The corium and concrete interface is reasonably reproduced.

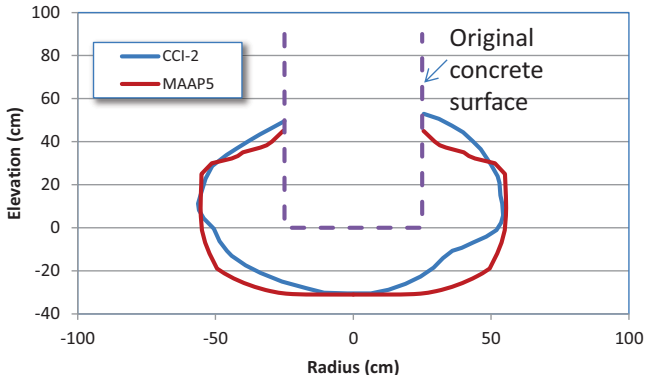

Figure 6. Comparison of shape of corium-concrete interface at the end of CCI-2 test.

4.2. CCI-3 Test

One of the observations in the CCI-3 experiment is that the lateral (sideward) ablation was much larger than the axial ablation. The cause of this phenomenon has not been fully understood, but it seems the theory regarding refractory crust formation is gaining support among the community of MCCI researchers. In this theory, refractory crusts formed at the bottom and the side in the beginning of the experiment. As the corium was continuously heated, the refractory crusts became thinner, until the sideward refractory crust failed. This caused concrete erosion in the sidewall and the concrete slag added into the corium pool lowered the corium temperature and the melting temperature. The downward refractory crust, however, survived for a long time, partially due to the melting temperature decrease following the side refractory crust failure. In the MAAP simulations of CCI-3, the adopted approach is to model a smaller downward heat transfer coefficient than the sideward heat transfer coefficient, to approximate the difference in the thermal resistances in the two directions. It is noted that in a reactor case, the downward and sideward ablation rates may be closer than the rates observed in the smaller scale experiments. The ratio of the sideward to downward ablation rates in a reactor case is still subject to more analyses and research.

Fig. 7(a) shows the comparisons of total heating power and the power into the molten corium for CCI-3. It is similar to the CCI-2 results in that the heating power is almost 100% in the molten corium before the water addition. After the water addition, the total heating power and the power into the molten corium both decrease. The power into the molten corium is about 10 kW less than the total power.

Fig. 7(b) shows comparisons of corium temperature for CCI-3. The experiment data shows a rapid temperature drop in the first 1000 seconds from 2200 K to about 1950 K. The temperature stays at about 2000 K from 1000 s until the water is added. MAAP results show a temperature increase to about 2400 K in the first 1500 s. It then slowly decreases to about 2000 K at the time of water addition. Again, this seems to indicate that the heat transfer coefficients used for CCI-3 are smaller than what are suggested by the experiment data. After water addition, the corium temperature without bulk cooling is very close to the experiment data. The corium temperature with bulk cooling shows a similar dip to the CCI-2 results, but the dip is much smaller compared to CCI-2.

Fig. 7(c) shows comparisons of ablation depth in the basemat and sidewalls. The ablation in the basemat of CCI-3 was highly non-uniform: the north-west (NW) quadrant and the center line started to ablate much later than other quadrants. Fig. 7(c) shows that the MAAP calculated axial ablation is closer to the ablation in the south-west (SW) quadrant which has the largest ablation depth in the basemat. The ablation in the sidewalls was also non-uniform: the south sidewall ablation is about 2 to 5 cm larger than the north sidewall ablation. The MAAP calculated sidewall ablation rate is closer to the north sidewall

ablation data. The total ablation depth calculated by MAAP agrees quite reasonably with the data. After water addition, the bulk cooling case exhibits a turn of the ablation depth curve, which is caused by the bulk cooling and temperature dip. Both cases produce reasonable ablation depths compared to the experiment data.

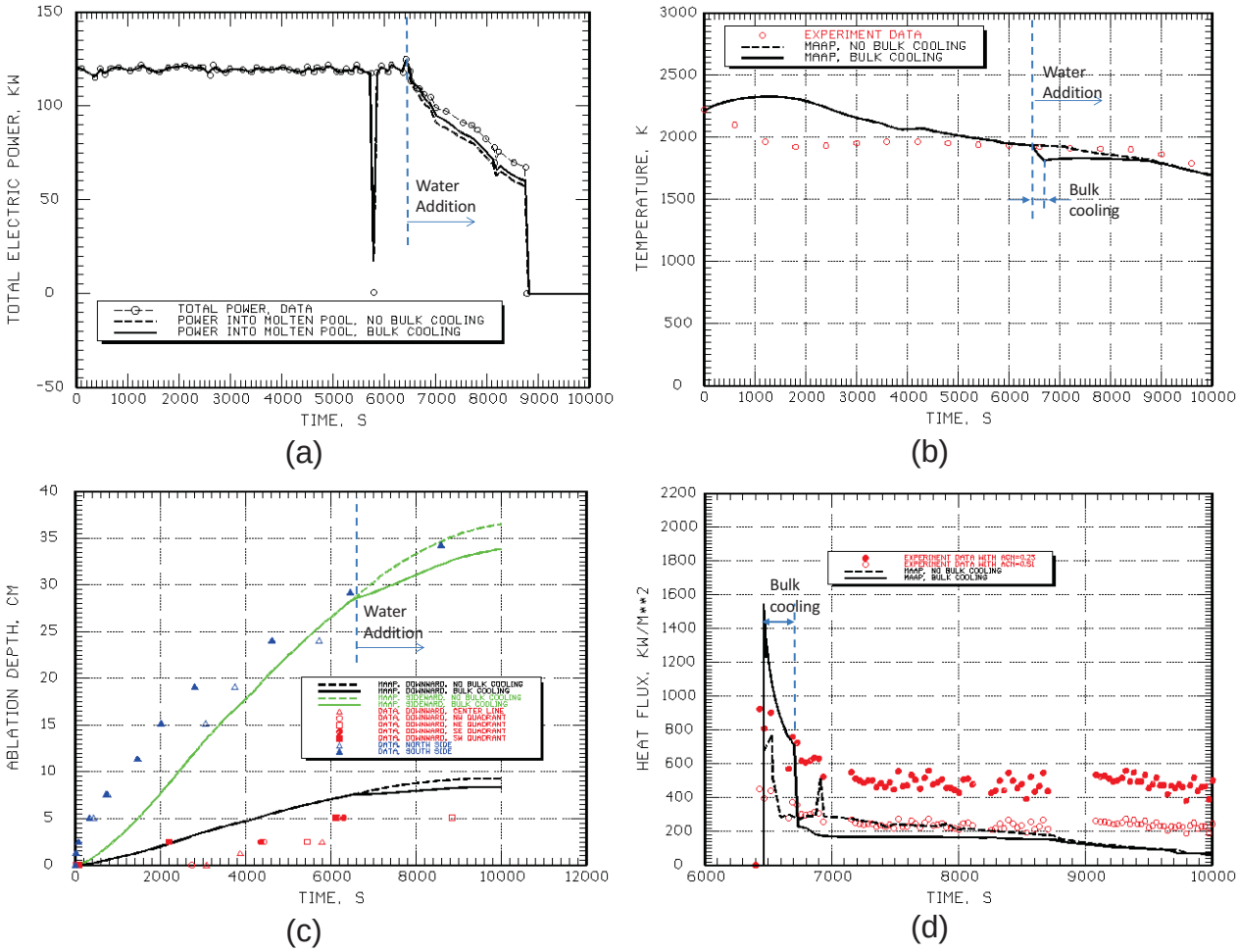

Figure 7. Comparisons of CCI-3 Test with and without bulk cooling model : (a) Heating power; (b) Corium temperature; (c) Ablation depth; (d) Heat flux to water.

Fig. 7(d) shows the comparison of the heat flux from corium to water for the CCI-3 test. In the CCI-3 test, the upper crust was anchored to the sidewall of the test section, and might have prevented water from contacting the entire corium top surface. Fig. 7(d) shows the heat fluxes based on two estimates of the heat transfer area. The heat transfer area ACN = 0.25 m^2 corresponds to the original (un-ablated) cross-sectional area, while ACN=0.51 m^2 corresponds to the surface area with the sideward ablation. The heat flux right after water addition is about 800 kW/m^2 for the case without bulk cooling. It then drops to about 300 kW/m^2 in about 100 s. The heat flux due to melt eruption is almost the same as the heat flux due to water ingression right after the water addition for the case without the bulk cooling. However, the heat flux due to melt eruption gradually decreases to almost zero, while the heat flux due to water ingression stays constant for the rest of the simulation. For the case with the bulk cooling model, the heat flux right after water addition is about 1.5 MW/m^2, which is much higher than the experiment data. The bulk cooling lasts only about 120 s. After the bulk cooling period, the heat flux drops to about 190

kW/m^2. The long term heat flux for the case with the bulk cooling is around 195 kW/m^2, which is slightly lower than the experimental data (based on a top surface area of 0.51 m^2).

It seems CCI-3 does not show a strong bulk cooling effect as opposed to the CCI-2 test. A potential reason for this weak bulk cooling effect might be that the abridged upper crust separated the water from the underlying molten corium pool. Perhaps water eventually still managed to pass through the crust to cool the corium pool, but bulk cooling did not occur. For this test, the case without bulk cooling is closer to the test condition than the case with bulk cooling. Despite the test condition differences, comparisons with both cases (with and without the bulk cooling model), are shown because the abridged crust is a phenomenon that is most likely limited to experimental scale. It is non-prototypic during severe accidents in nuclear power plants because the span of the crust in the reactor cavity/pedestal in nuclear plants is much larger than the span in MCCI experiments. For severe accidents in nuclear plants, a short bulk cooling period similar to what MAAP5.03+ calculates is likely to exist.

Fig. 8 compares the MAAP5.03+ calculated interface shape to experimental results. The MAAP calculated shape is symmetric, because it assumes identical ablation in the north and south sidewalls. The shape recorded in CCI-3 is asymmetric with the ablation in the south sidewall slightly larger than the ablation in the north sidewall. The general agreement of the shape between MAAP and CCI-3 is quite good.

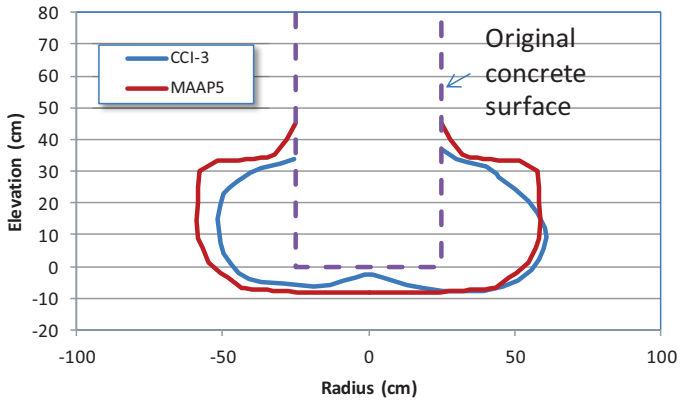

Figure 8. Comparison of shape of corium-concrete interface at the end of CCI-3 test.

5. CONCLUSION

Three new coolability models: water ingression, particle bed generation by melt eruption, and bulk cooling are modeled in the severe accident code MAAP5.03+. The details of these models have sufficiently discussed, and latest benchmarks presented. It has demonstrated that MAAP5.03+ can reasonably well calculate the major results of the CCI-2 and CCI-3 tests, including the power into the molten corium, corium temperature, ablation depth, heat flux into water, and shape of the corium-concrete interface. Some deviation has been noticed and analyzed. For example, the heat flux to water before 20,500 s in CCI-2 test. It is believed that the deviation is caused by sporadic melt eruptions for small but continuous ablations, which are currently ignored in the MAAP melt eruption model. Ignoring such conditions may yield more conservative results if the ablation rates are small. This has shown that the latest MAAP5.03+ code is a tool appropriate for MCCI and corium coolability analyses in nuclear power plants.

NOMENCLATURE

All variables have been defined in the text.

ACKNOWLEDGMENTS

This paper is based on work performed for the MAAP5 code enhancement project sponsored by EPRI and TOSHIBA [17].

REFERENCES

1. M.T. Farmer, D.J. Kilsdonk, R.W. Aeschlimann, "Corium Coolability under Ex-Vessel Accident Conditions for LWRs," *Nucl. Eng. Tech.*, **41**(5), pp. 575-602 (2009).
2. M.T. Farmer, S. Lomperski, D.J. Kilsdonk, R.W. Aeschlimann, S. Basu, "OECD MCCI Project: 2-D Core Concrete Interaction (CCI) Tests: Final Report," OECD/MCCI-2005-TR05, June, (2006).
3. Q. Zhou, C.Y. Paik, P.B. McMinn, "Benchmark of MCCI Model in MAAP5.02 against OECD CCI Experiment Series," *Proceedings of ICAPP-2014*, Charlotte, NC, April 6-9, (2014).
4. M.T. Farmer, J.J. Sienicki, B.W. Spencer, "CORQUENCH: A Model for Gas Sparging-Enhanced, Melt-Water, Film Boiling Heat Transfer," *ANS Winter Meeting on the Thermal Hydraulics of Severe Accidents*, Washington D.C., November 11-15, (1990).
5. M.T. Farmer, J.P. Schneider, B. Bonomo, G. Theofanous, B.W., Spencer, "Modeling and Database for Melt-Water Interfacial Heat Transfer," *Proc. of the 2nd OECD(NEA) CSNI Specialist Meeting on MCCI,* Karlsruhe, Germany, April 1-3, (1992).
6. P.J. Berenson, "Film Boiling Heat Transfer from a Horizontal Surface," *J. Heat Transfer*, **83**, pp. 351-357, (1961).
7. L.A. Bromley, "Heat Transfer in Stable Film Boiling," *Ph.D. Thesis*, Dept. of Chemistry, Univ. California, Berkeley, (1948).
8. W.D. Deckwer, "On the Mechanism of Heat Transfer in Bubble Column Reactors," *Chem. Eng. Sci.*, **35**, pp.1341-1346, (1980).
9. D.R. Topham, "The Deflection of an Ice Sheet by a Submerged Gas Source," *J. Applied Mech.*, **44**, pp.279-284, (1977).
10. M. Epstein, "Dryout heat flux during penetration of water into solidifying rock," *J. Heat transfer*, **128**, pp.847-850, (2006).
11. C.R.B. Lister, "On the Penetration of Water into Hot Rock," *Geophys. J. R. Astron Soc.*, **39**, pp. 465-509, (1974).
12. S. Lomperski, M.T. Farmer, "Experimental Evaluation of the Water Ingression Mechanism for Corium Cooling," *Nucl. Eng. Des.*, **237**, pp.905-917, (2007).
13. R.E. Henry, "Experiments on the Lower Plenum Response during a Sever Accident," Internal Memo of Fauske & Associates, LLC, (1993)
14. F.B. Ricou, D.B. Spalding, "Measurements of Entrainment by Axisymmetrical Turbulent Jets," *Journal of Fluid Mechanics*, **11**, pp.21-32, (1961)
15. R.J. Lipinski, "A particle-Bed Dryout Model with Upward and Downward Boiling," *Trans. of ANS*, **35**, pp. 358, (1980)
16. R.E. Henry, M. Epstein, H.K. Fauske, "Cooling of Debris Beds-Methods of Analyses for LWR Safety Assessments," *Proc. of the International Meeting on Thermal Nuclear Reactor Safety, NUREG/CP-0027*, Chicago, Aug 29~Sep.2, pp.1421~1432 (1982)
17. Electric Power Research Institute (EPRI), "Modular Accident Analysis Program (MAAP5) Containment Model Improvements: Japanese Fiscal Year (JFY) 2014 Project," *EPRI Product ID: 3002005028*, Published on March 13th, 2015